



Mapping the Energy Landscape from a Nanocrystal-Based Field Effect Transistor under Operation using Nanobeam Photoemission Spectroscopy

Mariarosa Cavallo, Erwan Bossavit, Huichen Zhang, Corentin Dabard, Tung Huu Dang, Adrien Khalili, Claire Abadie, Rodolphe Alchaar, Dario Mastrippolito, Yoann Prado, et al.

► To cite this version:

Mariarosa Cavallo, Erwan Bossavit, Huichen Zhang, Corentin Dabard, Tung Huu Dang, et al.. Mapping the Energy Landscape from a Nanocrystal-Based Field Effect Transistor under Operation using Nanobeam Photoemission Spectroscopy. *Nano Letters*, 2023, 23 (4), pp.1363-1370. 10.1021/acs.nanolett.2c04637 . hal-03954965

HAL Id: hal-03954965

<https://hal.science/hal-03954965>

Submitted on 24 Jan 2023

HAL is a multi-disciplinary open access archive for the deposit and dissemination of scientific research documents, whether they are published or not. The documents may come from teaching and research institutions in France or abroad, or from public or private research centers.

L'archive ouverte pluridisciplinaire **HAL**, est destinée au dépôt et à la diffusion de documents scientifiques de niveau recherche, publiés ou non, émanant des établissements d'enseignement et de recherche français ou étrangers, des laboratoires publics ou privés.

Mapping the Energy Landscape from a Nanocrystal-Based Field Effect Transistor under Operation using Nanobeam Photoemission Spectroscopy

Mariarosa Cavallo¹, Erwan Bossavit^{1,2}, Huichen Zhang¹, Corentin Dabard³, Tung Huu Dang^{1,4}, Adrien Khalili¹, Claire Abadie¹, Rodolphe Alchaar¹, Dario Matrippolito⁵, Yoann Prado¹, Loïc Becerra¹, Michael Rosticher⁴, Mathieu G. Silly², James K. Utterback¹, Sandrine Ithurria³, José Avila², Debora Pierucci⁶, Emmanuel Lhuillier^{1*}

¹ Sorbonne Université, CNRS, Institut des NanoSciences de Paris, INSP, F-75005 Paris, France.

² Synchrotron SOLEIL, L'Orme des Merisiers, Départementale 128, 91190 Saint-Aubin, France.

³ Laboratoire de Physique et d'Etude des Matériaux, ESPCI-Paris, PSL Research University, Sorbonne Université Univ Paris 06, CNRS UMR 8213, 10 rue Vauquelin 75005 Paris, France.

⁴ Laboratoire de Physique de l'Ecole normale supérieure, ENS, Université PSL, CNRS, Sorbonne Université, Université Paris-Diderot, Sorbonne Paris Cité, Paris, France Paris.

⁵ Department of Physical and Chemical Sciences (DSFC), University of L'Aquila, Via Vetoio, 67100 L'Aquila, Italy

⁶ Centre de Nanosciences et de Nanotechnologies, CNRS, Univ. Paris-Sud, Université Paris-Saclay, 10 Boulevard Thomas Gobert, 91120 Palaiseau, France

Abstract: As the field of nanocrystal-based optoelectronics matures, more advanced techniques must be developed in order to reveal the electronic structure of nanocrystals, particularly with device-relevant conditions. So far, most of the efforts have been focused on optical spectroscopy, and electrochemistry where an absolute energy reference is required. Device optimization requires probing not only the pristine material but also the material in its actual environment (*i.e.*, surrounded by a transport layer and an electrode, in the presence of an applied electric field). Here, we explored the use of photoemission microscopy as a strategy for *operando* investigation of NC-based devices. We demonstrate that the method can be applied to a variety of materials and device geometries. Finally, we show that it provides a direct access to the metal-semiconductor interface band bending as well as the distance over which the gate effect propagates in field-effect transistors.

Keywords: X-ray photoemission, field-effect transistor, nanocrystals, energy landscape.

*To whom correspondence should be sent: el@insp.upmc.fr

Nanocrystals (NCs), thanks to their broadly tunable optical features and electronic structure, are appealing building blocks for optoelectronics.¹ This has been demonstrated¹ in devices such as light-emitting diodes (LED), field-effect transistors (FET), and imaging sensors,^{2–5} with performances now competing with traditional epitaxially grown semiconductors.

The efficient integration of such new materials into devices strongly relies on the knowledge of the material's electronic structure.^{6–9} In the case of NCs, optical spectroscopy is certainly the most commonly used approach to probe a material's density of states. Time-resolved optical spectroscopy¹⁰ offers the highest temporal resolution down to a few tens of femtoseconds.⁹ Nevertheless, optical methods are only sensitive to the difference in population between the unoccupied and the occupied states. When an absolute energy measurement becomes necessary, electrochemistry^{11–14} and X-ray photoemission (XPS)^{15,16} are widely employed to determine band alignments. In particular, electrochemistry allows for the measurement of both the empty and occupied states, whereas XPS is often limited to the filled states due to the reduced efficiency of inverse photoemission. On the other hand, XPS studies^{17,18} are not limited to the states in the vicinity of the Fermi level and enable core-level investigation to unveil elemental redox states. Furthermore, when performed under synchrotron radiation, the incident energy can be tuned, allowing for discrimination of the bulk from the surface of the sample. In addition, some beamlines offer the possibility to focus the X-ray beam down to a few hundred nanometers. This enables the use of the XPS setup as a scanning microscope^{19–21} to image the energy landscape.^{21,22} Such microscopes are now used for the investigation of bulk semiconductors,^{24,25} 2D materials^{25–27} and their heterostructures,²⁸ or for perovskite materials²⁹ but remain unreported for NC-based devices. Nevertheless, they offer an interesting alternative to near-field microscopy methods such as STM^{30–33} and KPFM³⁴ while maintaining competitive spatial resolution.

This XPS-based microscopy method is applied here on a narrow band gap NC-based FET to probe *operando* the effect of drain and gate biases on the energy landscape of the confined semiconductor film. Furthermore, we highlight the capability of the method to directly observe the interfacial band bending at the electrode-NC interface or to explore the thickness dependence of the gate effect.

For illustration, the scanning soft X-ray photoemission microscopy is applied to a HgTe NC-based FET, see **Figure 1** and S1 to S4. Among existing NCs, HgTe NCs appear particularly suited for infrared optoelectronics³⁵ as shown in a wide range of devices³⁶: infrared cameras,^{2,37} spectrometers,^{38,39} phototransistors,^{40–42} (multicolor) photodiodes^{43–45} and light emitting devices.^{46,47} Because photoemission is a surface-sensitive method, it appears to be better suited for investigating devices with the active layer on top. To overcome this limitation and take advantage of the spatial resolution of the setup, we focus here on a planar transistor for its laterally accessible interfaces. The transistor is a dual-gated transistor where the dielectric part is made of an alumina layer, see **Figure 1a-b**. The channel is made of HgTe NCs, for which the size is chosen to lead to a ≈ 0.5 eV optical band gap, see **Figure 1d** and S5. The transfer curve of the transistor displays an ambipolar characteristic (**Figure 1c**), with both conduction of holes (under negative gate bias) and electrons (under positive gate bias).

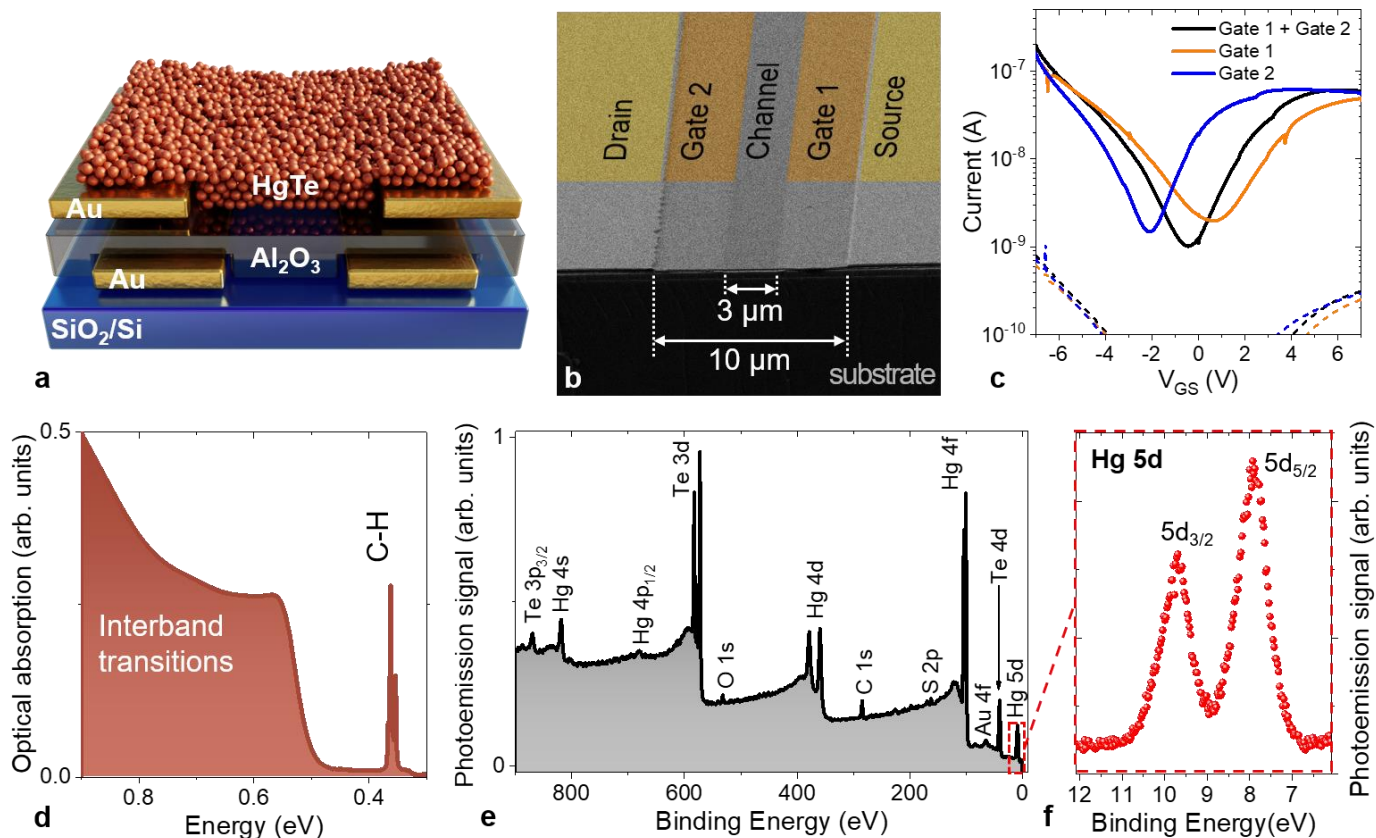


Figure 1 NC-based field-effect transistor. *a.* Scheme of the planar dual gated FET. *b.* Scanning electron microscopy image in false colors around the channel of the FET. *c.* Transfer curves (drain (full lines) and gate (dashed lines) currents as a function of the applied gate bias) under 1 V drain-source bias. *d.* Absorption spectrum of the HgTe NCs used as the channel of the FET. *e.* Survey photoemission spectrum of the HgTe NC used as channel for the FET. *f.* Photoemission spectrum of the Hg 5d state ($h\nu=95$ eV) used to map the energy landscape, which presents two contributions due to spin-orbit splitting.

The scanning soft X-ray photoemission microscope relies on the monochromatic X-ray beam of the synchrotron coupled to a zone plate to focus the photon beam, see **Figure 2a**. The latter behaves as a Fresnel lens and focuses the beam to achieve a ≈ 700 nm spot. Then, a point-by-point acquisition is conducted while scanning the sample, close to what is done in scanning electron microscopy. For each point, a photoemission spectrum is acquired, leading to a data set in the form of a 3D matrix where the kinetic energy completes the (x;y) mapping. The zone plate is typically made to operate at low energy (*i.e.*, to be compatible with angle-resolved photoemission). This constrains the material of interest to one that has a core level below 100 eV. Here we look at two materials: HgTe (Figure S5-S7) and PbS (Figure S8-11), both of which present 5d states at low binding energy (BE) (at 8 eV for Hg 5d, see **Figure 1e-f** and S6, and 19.1 eV for Pb 5d, see Figure S9). Note that other materials conventionally used for colloidal nanocrystals would likewise exhibit states with low BEs (BE(Cd 4d) ≈ 10 eV, BE(Ag 4p) ≈ 57 eV, BE(In 4d) ≈ 17 eV, BE(Cu 3p) ≈ 76 eV...), therefore the method should be quite general. It remains nevertheless crucial to design a device in which photo-charging effects induced by the photoemission process are low (*i.e.* using conductive channel and electrodes without insulating passivation) to actually allocate the effect to device operation and not to the building of the electrostatic charges.

In addition to the scanning mode, the microscope enables *operando* investigation of the device through the application of bias directly inside the analysis chamber. As a result, the microscope can be used to probe the energy landscape of a wide range of NC-based devices while they are operating, with a sub- μm resolution.

The method is first applied on a grounded device (*i.e.*, drain, source, and both gates are grounded) to directly observe interfacial band bending. We acquire a map of the intensity of the Hg 5d doublet (Hg 5d_{5/2} – Hg 5d_{3/2} spin-orbit separation = 1.8 eV) around the channel area with a step size of 1 μm , see **Figure 2b**. This map, where each pixel corresponds to a Hg 5d spectrum, reflects a shift of the Hg 5d state across the channel. By integrating the map over the y direction along the length of the channel, we can obtain a map of the binding energy as a function of the coordinate across the channel, see **Figure 2c**. The map clearly shows a shift of the Hg 5d peaks to higher binding energies across the drain-source channel between 5 μm and -5 μm relative to the center of the channel. To better visualize this energy shift, we fit the Hg 5d core level peaks and plot a profile of the peak energy in **Figure 2d** (only the fitting of the Hg 5d_{5/2} component was represented). We could be inclined to attribute this shift to a photo-charging of the film since, in the channel area, the film no longer overlaps with metallic electrodes. However, this hypothesis can be ruled out since charging effects would lead to peak broadening toward higher binding energy, whereas here the Hg 5d_{5/2} state keeps the same linewidth (see Figure S12). We can thus confidently attribute the observed shift to interfacial band bending at the lateral metal-semiconductor interface. The observed shift can be used to estimate the electron density in the material. At the interface between the metal and the semiconductor, the band bending is expected to follow a parabolic shape⁴⁸ $V(x) = \frac{en}{2\varepsilon_r\varepsilon_0}x^2 + ax + b$

where e is the elementary charge, n the carrier density, ε_r the dielectric constant and ε_0 the vacuum permittivity, while a and b are fitting parameters that depend on the geometry. Assuming $\varepsilon_r = 15$,⁴⁹ we can estimate n to be $2.6 \times 10^{13} \text{ cm}^{-3}$. If we consider a spherical shape for the particle of a given radius R , we can estimate the NC density assuming a randomly close packing (*i.e.*, packing density of 0.64) as $N_{NC} = \frac{0.64}{4/3\pi R^3} = 1.2 \times 10^{18} \text{ NC.cm}^{-3}$, meaning that there is 2×10^{-5} electron per HgTe NC.

From this value, we can then calculate the activation energy and estimate qualitatively the residual doping for the material. If we assume that the conduction band in HgTe is doubly degenerate,⁵⁰ the thermally activated carrier density per NC is given by $2 \cdot \exp\left(\frac{-E_a}{k_b T}\right)$ with k_b the Boltzmann constant, $T=250 \text{ K}$ the temperature and E_a the activation energy. To reach a density of 2×10^{-5} electrons per NC through thermal excitation, a 250 meV activation energy is required, which is very close to the half band gap value. This result is consistent with X-ray photoemission measurements (Figure S7) that show that the Fermi level of the material is also close to the middle of the 500 meV band-gap. The residual doping in the studied particles thus appears very low, making the material relevant for photodetection.

To demonstrate the generality of the method, we then apply it to the same device structure where the channel is instead made of PbS NCs with a band gap around telecom wavelength ($E_G=0.8 \text{ eV}$ or $1.5 \mu\text{m}$, see Figure S8). Aside from their chemical nature, both materials also differ in their doping. Whereas HgTe presents a quasi-intrinsic behaviour, PbS is strongly n -doped with a Fermi level and conduction band that are almost degenerate for this band gap value and short thiol capping ligands, see Figure S10-S11. In the PbS based devices, no band bending is observed, see Figure S15. The PbS NCs are 8 nm in size, and assuming they are randomly close-packed (*i.e.*, packing density of 0.64), we can estimate the carrier density to be $n = \frac{8 \times 0.64}{4/3\pi R^3} \approx 10^{19} \text{ cm}^{-3}$ (for PbS the conduction band is 8-fold degenerate⁵¹). The screening length is expected to scale as $n^{-1/2}$. Thus, with a carrier density 10^6 times higher, the band bending is supposed to occur over a 1000 times shorter distance than for HgTe NCs. With HgTe, the band curvature was observed over a few μm (**Figure 2c-d**), and with PbS, it should be as short as a few nm, which is far smaller than the focus beam spot of our experiment. The absence of observed band bending is thus expected for strongly doped PbS, as shown in Figure S15.

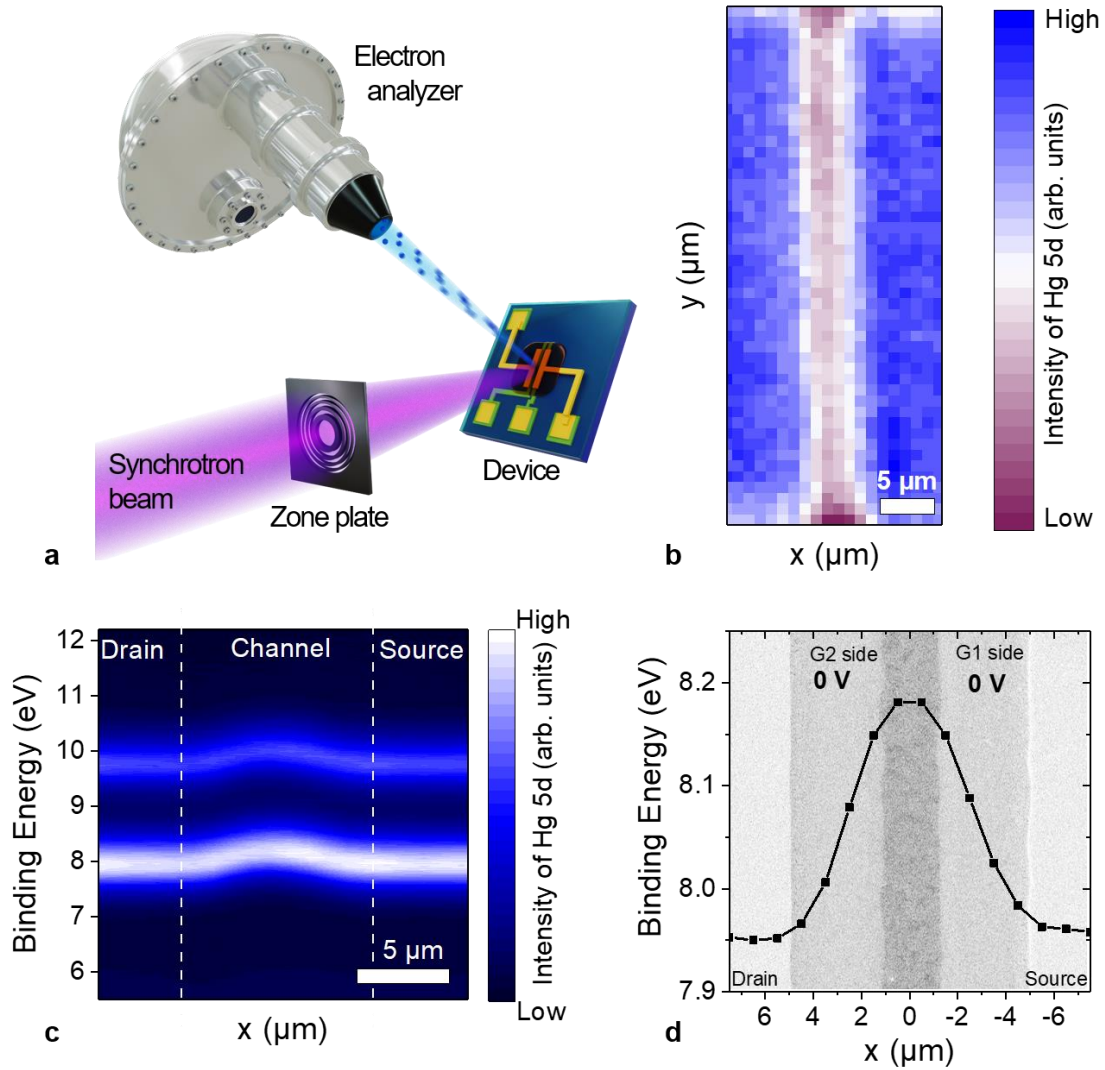


Figure 2 X-ray photoemission microscope and band bending. *a.* Schematic of the X-ray photoemission microscope. A soft X-ray beam from the synchrotron is focused on the sample with sub- μm resolution thanks to the zone plate (i.e., Fresnel lens). The photoemission signal is acquired point by point in a scanning mode with a hemispherical electron analyzer. *b.* Intensity of the Hg 5d states along the drain-source channel for the transistor device, all electrodes grounded. *c.* Integrated binding energy of the Hg 5d state doublet along the drain-source channel. Dashed lines highlight the position of the channel. *d.* Fitting results of the binding energy position of the Hg 5d_{5/2} state along the drain-source channel. For clarity in the background of figure (d), we report a scanning electron microscopy image of the device to highlight the location of the channel area.

It is worth pointing out that direct measurements of the band bending and of the interface barriers are usually complicated to obtain using optical methods that are only sensitive to the difference in energy between the valence and conduction bands. In contrast, using a scanning soft X-ray photoemission microscope, we have a direct measurement of this value, which can be used to determine material carrier density.

Now that the grounded energy potential is understood, we can see how the profile is affected by the application of electric fields, starting with a drain-source bias, see **Figure 3**. We first follow the energy landscape induced by the application of a drain-source bias over the FET channel while the gates remain grounded. A map depicting the Hg 5d states intensity is shown in **Figure 3b**. It shows a strong difference in the energy position of the peak between the two electrodes. A profile of this energy position across the channel is given in **Figure 3c**. Above a given electrode, the potential is

homogeneous (Figure S13), and we quantify the fluctuation of potential⁵² to be smaller than 28 meV. This is close to the thermal energy (21 meV) for the measurement conducted at 250 K and similar to the energy resolution of the setup. Over the channel, the binding energy of the Hg 5d increases by 5 eV (**Figure 3c** and S14), which exactly matches the 5 V applied bias over the two electrodes. One can note that the energy drop presents a smooth profile (*i.e.* no discrete drop that may be connected to the discrete charge content of a NC), that we attribute to the averaging of the signal over a large number of NC (>10000 NCs below the beam). Furthermore, the energy drop occurs over the whole channel and not only at the metal interface, suggesting the formation of ohmic contacts. This potential profile is also compared to an electrostatic simulation (Figure S16), and we obtain good agreement for the magnitude of the electric field as long as the channel length is made 1 μm shorter than its nominal value, which is compatible with the inaccuracy expected from the multiple lithography process.

To further demonstrate that the *operando* scanning soft X-ray photoemission microscopy can be applied to several materials (HgTe and PbS), we also test its potential for other geometries of electrodes. Interdigitated electrodes are conventionally used to probe conduction in a NC array. Here such a geometry has been fabricated on a conventional Si/SiO₂ wafer, see **Figure 3d**. Under 1 V of applied bias, a strong contrast in the energy of the Hg 5d states appears between two consecutive digits, see **Figure 3e** and f.

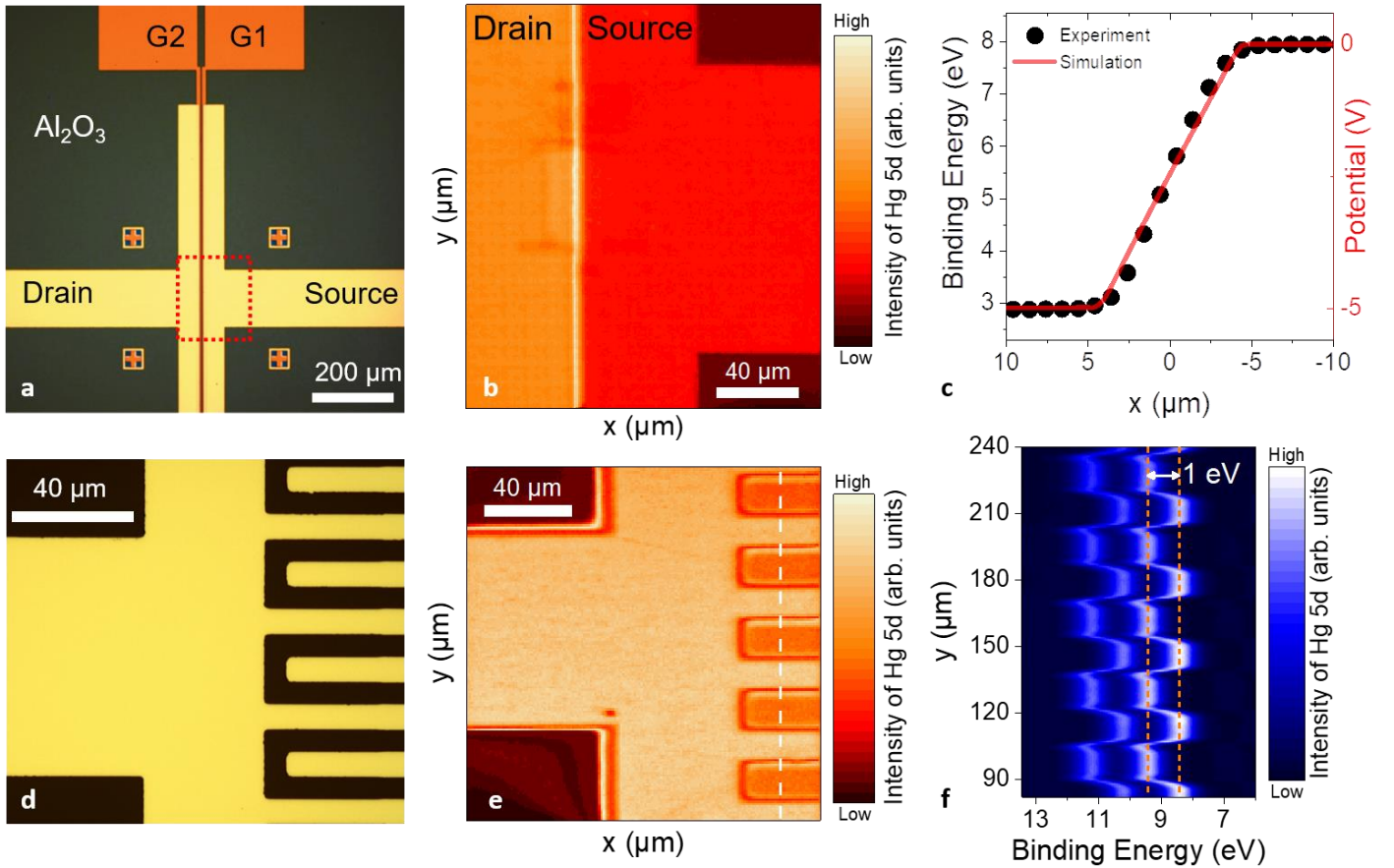


Figure 3 Effect of drain-source bias. a. Optical microscopy image of dual-gate FET with channel made of a HgTe NC film. The dashed red rectangle corresponds to the area probed in part b. b. Intensity map of the Hg 5d states ($h\nu=95$ eV) over the channel of the FET while a 5 V bias is applied over the drain-source electrodes. c. Binding energy profile of the Hg 5d_{5/2} state ($h\nu=95$ eV) along the drain-source electrode. The full line is the simulated potential profile obtained from the electrostatic simulation of the structure. d. Optical microscopy image of interdigitated electrodes coated with a HgTe NC film. e. Intensity map of the Hg 5d states ($h\nu=95$ eV) once a 1 V bias is applied between the pair of the interdigitated electrodes coated with an HgTe NC thin film. The dashed line corresponds to the line along which the profile of part f is acquired. f. Profile of the

binding energy of the Hg 5d states ($h\nu=95$ eV) over the digits of the electrode while a 1 V drain-source bias is applied.

To complete the *operando* study of the device, we investigate the effect of the application of gate bias. Such measurements are of strong interest for the design of phototransistors. Compared to other device geometries (photoconductor and diode), the transistor offers post-fabrication tunability. The gate can be used to control the carrier density, which affects the dark current magnitude as well as the device's responsivity. However, designing phototransistors represents a tradeoff. On the one hand, thicker films are better for increasing light absorption. On the other hand, the gate effect is a surface effect, and thicker films also reduce its amplitude. It is thus crucial to determine the critical NC film thickness for the gate to be effective.

Figure 4a depicts the binding energy profile of the Hg 5d doublet across the transistor channel while a -6V gate bias is applied and it clearly contrasts with the profile using grounded electrodes (**Figure 2d**). While with grounded electrodes the profile presents upward band bending (**Figure 2c**), here we clearly observe a downward bump that spatially overlaps with the activated gate 1. The change in the energy landscape for various values of gate bias is given in **Figure 4b**. The nonlinearity of the profile shift with bias suggests that some charges are used to passivate the dielectric dangling bonds before effectively gating the NCs. Such an observation is consistent with the presence of a hysteresis observed in the transistor transfer curves, see **Figure S3**. The magnitude of the shift (Δ B.E. up to ≈ 0.4 eV) is also larger than the initial band bending around ≈ 0.2 eV, see **Figure 2d**. It is thus possible to shift the Fermi level on both, the upper (to achieve electron injection) and lower part (to obtain hole injection) of the band gap. This observation is consistent with the ambipolar character of the FET, where both electron injection (valence band moves away from the Fermi level) and hole injection (valence band moves toward the Fermi level) are observed, see **Figure 1c**.

Finally, we measured how the effect of gate bias on the energy landscape changes with film thickness. We found that the magnitude of gate-induced energy shift Δ B.E. decreases as the film thickness increases, see **Figure 4c**. An exponential fit of this decay, assuming that the effect should collapse at a long distance (*i.e.*, Δ B.E. ($t=\infty$) = 0 eV), leads to a 75 nm characteristic length over which the gate is active, which corresponds to 5-10 NC layers. This remains far shorter than the material absorption depth⁵³ (>1 μ m), but it shows that films of around hundred nm can still be used to design phototransistors and combine both light absorption and carrier density modulation.

The Debye length $\lambda_D = \sqrt{\frac{\epsilon_0 \epsilon_r k_B T}{ne^2}}$ provides the distance over which screening occurs. If the film remained intrinsic with $n=2 \times 10^{13} \text{ cm}^{-3}$, Debye length as long as 830 nm would be possible. However, when the FET is under operation, the carrier density rises and screening gets more efficient. From the transfer curve (**Figure 1c**), we observe a rise of the current by a factor 100 under gate application. If we assume that in a FET, the rise of current is fully the result of an increase of carrier density (*i.e.* neglecting the carrier density dependence of the mobility), gate should tune the carrier density by hundred and thus reduces the Debye length by a factor 10, leading to a value around ≈ 80 nm, very close to the decay length observed experimentally.

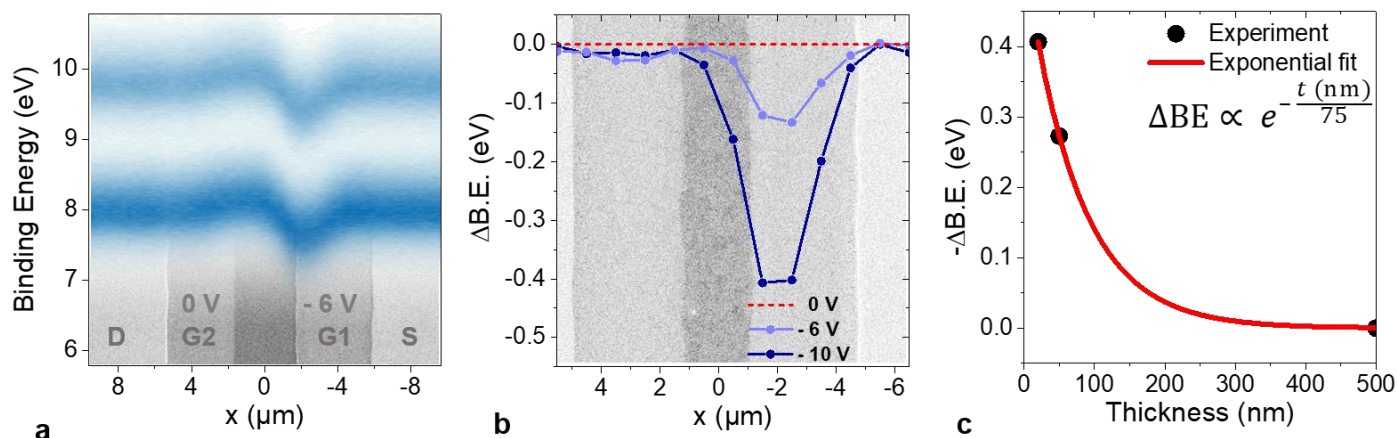


Figure 4 Effect of gate bias. *a.* Profile of the binding energy of the Hg 5d states ($h\nu=95$ eV) over the channel of the FET while a -6 V gate bias is applied over the gate G_1 vs source electrode. A scanning electron microscopy image of the device is superimposed to correlate the variation of kinetic energy with the gate location. *b.* Profile of the gate-induced binding energy change (the profile under 0 V is subtracted, see **Figure 2d**) along the channel, while two values of gate bias are applied. *c.* Magnitude of the gate induced shift of the energy landscape as a function of the film thickness.

In summary, we have used scanning soft X-ray photoemission microscopy as a tool to reveal the energy landscape in nanocrystal-based devices. This technique has very few constraints on the material of interest and can be applied to a large range of geometries (FET, interdigitated electrodes). This method gives direct access to the interface band bending at the micrometric scale, which is usually tricky to reveal using traditional optical methods. This approach can also be used to study the device under operation (*operando* measurements) to unveil the effect of the applied drain and gate electric fields. Using this method, we were able to estimate the length over which the gate effect can propagate through the thickness of a HgTe NC film, which is critical in the design of phototransistors used for infrared sensing.

ASSOCIATED CONTENT

Supporting information includes (i) method for synthesis, material characterization, device fabrication, *in situ* X-ray photoemission microscopy, (ii) electrical properties of the HgTe NC-based FET, (iii) additional data from X-ray photoemission microscopy, (iv) electrostatic modelling of the drain source bias.

COMPETING INTEREST

The authors declare no competing financial interest.

ACKNOWLEDGMENTS

Authors thanks Abhay Shukla for suggesting the project. The project is supported by ERC starting grant blackQD (grant n° 756225). We acknowledge the use of clean-room facilities from the “Centrale de Proximité Paris-Centre”. This work is supported by grants: IPER-Nano2 (ANR-18CE30-0023-01), Copin (ANR-19-CE24-0022), Frontal (ANR-19-CE09-0017), Graskop (ANR-19-CE09-0026), NITQuantum (ANR-20-ASTR-0008-01), Bright (ANR-21-CE24-0012-02), MixDferro (ANR-21-CE09-0029), QuickTera (ANR-22-CE09-0018) and Operatwist (ANR-22-CE09).

REFERENCES

- (1) Liu, M.; Yazdani, N.; Yarema, M.; Jansen, M.; Wood, V.; Sargent, E. H. Colloidal Quantum Dot Electronics. *Nat. Electron.* **2021**, *4* (8), 548–558.
- (2) Gréboval, C.; Darson, D.; Parahyba, V.; Alchaar, R.; Abadie, C.; Noguier, V.; Ferré, S.; Izquierdo, E.; Khalili, A.; Prado, Y.; Potet, P.; Lhuillier, E. Photoconductive Focal Plane Array Based on HgTe Quantum Dots for Fast and Cost-Effective Short-Wave Infrared Imaging. *Nanoscale* **2022**, *14* (26), 9359–9368.
- (3) Malinowski, P. Building Low-Cost Infrared Sensors with Sub-Micron Films. *Imaging Mach. Vis. Eur.* **2019**, *93*, 16–18.
- (4) Steckel, J. S.; Josse, E.; Pattantyus-Abraham, A. G.; Bidaud, M.; Mortini, B.; Bilgen, H.; Arnaud, O.; Allegret-Maret, S.; Saguin, F.; Mazet, L.; Lhostis, S.; Berger, T.; Haxaire, K.; Chapelon, L. L.; Parmigiani, L.; Gouraud, P.; Brihoum, M.; Bar, P.; Guillermet, M.; Favreau, S.; Duru, R.; Fantuz, J.; Ricq, S.; Ney, D.; Hammad, I.; Roy, D.; Arnaud, A.; Vianne, B.; Nayak, G.; Virollet, N.; Farys, V.; Malinge, P.; Tournier, A.; Lalanne, F.; Crocherie, A.; Galvier, J.; Rabary, S.; Noblanc, O.; Wehbe-Alause, H.; Acharya, S.; Singh, A.; Meitzner, J.; Aher, D.; Yang, H.; Romero, J.; Chen, B.; Hsu, C.; Cheng, K. C.; Chang, Y.; Sarmiento, M.; Grange, C.; Mazaleyrat, E.; Rochereau, K. 1.62 μm Global Shutter Quantum Dot Image Sensor Optimized for Near and Shortwave Infrared. In *2021 IEEE International Electron Devices Meeting (IEDM)*; 2021; p 23.4.1-23.4.4.
- (5) Gregory, C.; Hilton, A.; Violette, K.; Klem, E. 66-3: Invited Paper: Colloidal Quantum Dot Photodetectors for Large Format NIR, SWIR, and ESWIR Imaging Arrays. *SID Symp. Dig. Tech. Pap.* **2021**, *52*, 982–986.
- (6) Yazdani, N.; Andermatt, S.; Yarema, M.; Farto, V.; Bani-Hashemian, M. H.; Volk, S.; Lin, W. M. M.; Yarema, O.; Luisier, M.; Wood, V. Charge Transport in Semiconductors Assembled from Nanocrystal Quantum Dots. *Nat. Commun.* **2020**, *11* (1), 2852.
- (7) Sneyd, A. J.; Beljonne, D.; Rao, A. A New Frontier in Exciton Transport: Transient Delocalization. *J. Phys. Chem. Lett.* **2022**, *13* (29), 6820–6830.
- (8) Ginsberg, N. S.; Tisdale, W. A. Busting through Quantum Dot Barriers. *Nat. Mater.* **2022**, *21* (5), 497–499.
- (9) Zhang, Z.; Sung, J.; Toolan, D. T. W.; Han, S.; Pandya, R.; Weir, M. P.; Xiao, J.; Dowland, S.; Liu, M.; Ryan, A. J.; Jones, R. A. L.; Huang, S.; Rao, A. Ultrafast Exciton Transport at Early Times in Quantum Dot Solids. *Nat. Mater.* **2022**, *21* (5), 533–539.
- (10) Shcherbakov-Wu, W.; Tisdale, W. A. A Time-Domain View of Charge Carriers in Semiconductor Nanocrystal Solids. *Chem. Sci.* **2020**, *11* (20), 5157–5167.
- (11) Ravi, V. K.; Markad, G. B.; Nag, A. Band Edge Energies and Excitonic Transition Probabilities of Colloidal CsPbX₃ (X = Cl, Br, I) Perovskite Nanocrystals. *ACS Energy Lett.* **2016**, *1* (4), 665–671.
- (12) Amelia, M.; Lincheneau, C.; Silvi, S.; Credi, A. Electrochemical Properties of CdSe and CdTe Quantum Dots. *Chem. Soc. Rev.* **2012**, *41* (17), 5728–5743.
- (13) Puntambekar, A.; Wang, Q.; Miller, L.; Smieszek, N.; Chakrapani, V. Electrochemical Charging of CdSe Quantum Dots: Effects of Adsorption versus Intercalation. *ACS Nano* **2016**, *10* (12), 10988–10999.
- (14) Chen, M.; Guyot-Sionnest, P. Reversible Electrochemistry of Mercury Chalcogenide Colloidal Quantum Dot Films. *ACS Nano* **2017**, *11* (4), 4165–4173.
- (15) Jagtap, A.; Martinez, B.; Goubet, N.; Chu, A.; Livache, C.; Gréboval, C.; Ramade, J.; Amelot, D.; Trouset, P.; Triboulin, A.; Ithurria, S.; Silly, M. G.; Dubertret, B.; Lhuillier, E. Design of a Unipolar Barrier for a Nanocrystal-Based Short-Wave Infrared Photodiode. *ACS Photonics* **2018**, *5* (11), 4569–4576.
- (16) Brown, P. R.; Kim, D.; Lunt, R. R.; Zhao, N.; Bawendi, M. G.; Grossman, J. C.; Bulović, V. Energy Level Modification in Lead Sulfide Quantum Dot Thin Films through Ligand Exchange. *ACS Nano* **2014**, *8* (6), 5863–5872.
- (17) Spencer, B. F.; Cliffe, M. J.; Graham, D. M.; Hardman, S. J. O.; Seddon, E. A.; Syres, K. L.; Thomas, A. G.; Sirotti, F.; Silly, M. G.; Akhtar, J.; O'Brien, P.; Fairclough, S. M.; Smith, J. M.; Chattopadhyay, S.; Flavell, W. R. Dynamics in Next-Generation Solar Cells: Time-Resolved Surface Photovoltage Measurements of Quantum Dots Chemically Linked to ZnO (1010). *Faraday Discuss* **2014**, *171*, 275–298.

- (18) Spencer, B. F.; Cliffe, M. J.; Graham, D. M.; Hardman, S. J. O.; Seddon, E. A.; Syres, K. L.; Thomas, A. G.; Sirotti, F.; Silly, M. G.; Akhtar, J.; O'Brien, P.; Fairclough, S. M.; Smith, J. M.; Chattopadhyay, S.; Flavell, W. R. Chemically-Specific Time-Resolved Surface Photovoltage Spectroscopy: Carrier Dynamics at the Interface of Quantum Dots Attached to a Metal Oxide. *Surf. Sci.* **2015**, *641*, 320–325.
- (19) Escher, M.; Winkler, K.; Renault, O.; Barrett, N. Applications of High Lateral and Energy Resolution Imaging XPS with a Double Hemispherical Analyser Based Spectromicroscope. *J. Electron Spectrosc. Relat. Phenom.* **2010**, *178–179*, 303–316.
- (20) Renault, O. High-Resolution XPS Spectromicroscopy. *Surf. Interface Anal.* **2010**, *42* (6–7), 816–825.
- (21) Avila, J.; Asensio, M. C. First NanoARPES User Facility Available at SOLEIL: An Innovative and Powerful Tool for Studying Advanced Materials. *Synchrotron Radiat. News* **2014**, *27* (2), 24–30.
- (22) Blomfield, C. J. Spatially Resolved X-Ray Photoelectron Spectroscopy. *J. Electron Spectrosc. Relat. Phenom.* **2005**, *143* (2), 241–249.
- (23) Majchrzak, P.; Muzzio, R.; Jones, A. J.; Curcio, D.; Volckaert, K.; Biswas, D.; Gobbo, J.; Singh, S.; Robinson, J. T.; Watanabe, K. In Operando Angle-Resolved Photoemission Spectroscopy with Nanoscale Spatial Resolution: Spatial Mapping of the Electronic Structure of Twisted Bilayer Graphene. *Small Sci.* **2021**, *1* (6), 2000075.
- (24) Barrett, N.; Gottlob, D. M.; Mathieu, C.; Lubin, C.; Passicouset, J.; Renault, O.; Martinez, E. Operando X-Ray Photoelectron Emission Microscopy for Studying Forward and Reverse Biased Silicon p-n Junctions. *Rev. Sci. Instrum.* **2016**, *87* (5), 053703.
- (25) Hu, A.; Liu, W.; Li, X.; Xu, S.; Li, Y.; Xue, Z.; Tang, J.; Ye, L.; Yang, H.; Li, M.; Ye, Y.; Sun, Q.; Gong, Q.; Lu, G. Spectromicroscopy and Imaging of Photoexcited Electron Dynamics at In-Plane Silicon Pn Junctions. *Nanoscale* **2021**, *13* (4), 2626–2631.
- (26) Joucken, F.; Avila, J.; Ge, Z.; Quezada-Lopez, E. A.; Yi, H.; Le Goff, R.; Baudin, E.; Davenport, J. L.; Watanabe, K.; Taniguchi, T. Visualizing the Effect of an Electrostatic Gate with Angle-Resolved Photoemission Spectroscopy. *Nano Lett.* **2019**, *19* (4), 2682–2687.
- (27) Lavayssière, M.; Renault, O.; Mariolle, D.; Veillerot, M.; Barnes, J. P.; Hartmann, J. M.; Leroy, J.; Barrett, N. Photoemission Induced Bias in Two-Dimensional Silicon Pn Junctions. *Appl. Phys. Lett.* **2011**, *99* (20), 202107.
- (28) Renault, O.; Kim, H.; Dumcenco, D.; Unuchek, D.; Chevalier, N.; Gay, M.; Kis, A.; Fairley, N. Correlating Chemical and Electronic States from Quantitative Photoemission Electron Microscopy of Transition-Metal Dichalcogenide Heterostructures. *J. Vac. Sci. Technol. A* **2021**, *39* (5), 053210.
- (29) Cattelan, M.; Fox, N. A. A Perspective on the Application of Spatially Resolved ARPES for 2D Materials. *Nanomaterials* **2018**, *8* (5), 284.
- (30) Dunfield, S. P.; Bojar, A.; Cacovich, S.; Frégnaux, M.; Klein, T.; Bramante, R.; Zhang, F.; Regaldo, D.; Dufoulon, V.; Puel, J.-B.; Teeter, G.; Luther, J. M.; Bouttemy, M.; Nordlund, D.; Zhu, K.; Moore, D. T.; van Hest, M. F. A. M.; Kleider, J.-P.; Berry, J. J.; Schulz, P. Carrier Gradients and the Role of Charge Selective Contacts in Lateral Heterojunction All Back Contact Perovskite Solar Cells. *Cell Rep. Phys. Sci.* **2021**, *2* (8), 100520.
- (31) Peric, N.; Lambert, Y.; Singh, S.; Khan, A. H.; Franchina Vergel, N. A.; Deresmes, D.; Berthe, M.; Hens, Z.; Moreels, I.; Delerue, C. Van Hove Singularities and Trap States in Two-Dimensional CdSe Nanoplatelets. *Nano Lett.* **2021**, *21* (4), 1702–1708.
- (32) Swart, I.; Liljeroth, P.; Vanmaekelbergh, D. Scanning Probe Microscopy and Spectroscopy of Colloidal Semiconductor Nanocrystals and Assembled Structures. *Chem. Rev.* **2016**, *116* (18), 11181–11219.
- (33) Evers, W. H.; Schins, J. M.; Aerts, M.; Kulkarni, A.; Capiod, P.; Berthe, M.; Grandidier, B.; Delerue, C.; Van Der Zant, H. S.; Van Overbeek, C. High Charge Mobility in Two-Dimensional Percolative Networks of PbSe Quantum Dots Connected by Atomic Bonds. *Nat. Commun.* **2015**, *6* (1), 1–8.
- (34) Millo, O.; Katz, D.; Cao, Y.; Banin, U. Imaging and Spectroscopy of Artificial-Atom States in Core/Shell Nanocrystal Quantum Dots. *Phys. Rev. Lett.* **2001**, *86* (25), 5751.

- (35) Zhang, Y.; Zhrebetskyy, D.; Bronstein, N. D.; Barja, S.; Lichtenstein, L.; Schuppisser, D.; Wang, L.-W.; Alivisatos, A. P.; Salmeron, M. Charge Percolation Pathways Guided by Defects in Quantum Dot Solids. *Nano Lett.* **2015**, *15* (5), 3249–3253.
- (36) Gréboval, C.; Chu, A.; Goubet, N.; Livache, C.; Ithurria, S.; Lhuillier, E. Mercury Chalcogenide Quantum Dots: Material Perspective for Device Integration. *Chem. Rev.* **2021**, *121* (7), 3627–3700.
- (37) Nakotte, T.; Munyan, S. G.; Murphy, J. W.; Hawks, S. A.; Kang, S.; Han, J.; Hiszpanski, A. M. Colloidal Quantum Dot Based Infrared Detectors: Extending to the Mid-Infrared and Moving from the Lab to the Field. *J. Mater. Chem. C* **2022**, *10* (3), 790–804.
- (38) Tang, X.; Zhang, S.; Bi, C.; Qin, T.; Liu, Y.; Cao, J.; Song, J.; Huo, Y.; Chen, M.; Hao, Q. *Wafer-Scale Fabrication of CMOS-Compatible Trapping-Mode Infrared Imagers with Colloidal Quantum Dots*; preprint; In Review, 2022. <https://www.researchsquare.com/article/rs-2076887/v1> (accessed 2022-11-03).
- (39) Wen, C.; Zhao, X.; Mu, G.; Chen, M.; Tang, X. Simulation and Design of HgSe Colloidal Quantum-Dot Microspectrometers. *Coatings* **2022**, *12* (7), 888.
- (40) Grotevent, M. J.; Yakunin, S.; Bachmann, D.; Romero, C.; Vázquez de Aldana, J. R.; Madi, M.; Calame, M.; Kovalenko, M. V.; Shorubalko, I. Integrated Photodetectors for Compact Fourier-Transform Waveguide Spectrometers. *Nat. Photonics* **2022**, 1–6.
- (41) Dong, Y.; Chen, M.; Yiu, W. K.; Zhu, Q.; Zhou, G.; Kershaw, S. V.; Ke, N.; Wong, C. P.; Rogach, A. L.; Zhao, N. Solution Processed Hybrid Polymer: HgTe Quantum Dot Phototransistor with High Sensitivity and Fast Infrared Response up to 2400 nm at Room Temperature. *Adv. Sci.* **2020**, *7* (12), 2000068.
- (42) Gréboval, C.; Chu, A.; Magalhaes, D. V.; Ramade, J.; Qu, J.; Rastogi, P.; Khalili, A.; Chee, S.-S.; Aubin, H.; Vincent, G.; Bals, S.; Delerue, C.; Lhuillier, E. Ferroelectric Gating of Narrow Band-Gap Nanocrystal Arrays with Enhanced Light–Matter Coupling. *ACS Photonics* **2021**, *8* (1), 259–268.
- (43) Chen, M.; Lu, H.; Abdelazim, N. M.; Zhu, Y.; Wang, Z.; Ren, W.; Kershaw, S. V.; Rogach, A. L.; Zhao, N. Mercury Telluride Quantum Dot Based Phototransistor Enabling High-Sensitivity Room-Temperature Photodetection at 2000 nm. *ACS Nano* **2017**, *11* (6), 5614–5622.
- (44) Tang, X.; Ackerman, M. M.; Chen, M.; Guyot-Sionnest, P. Dual-Band Infrared Imaging Using Stacked Colloidal Quantum Dot Photodiodes. *Nat. Photonics* **2019**, *13* (4), 277–282.
- (45) Ackerman, M. M.; Tang, X.; Guyot-Sionnest, P. Fast and Sensitive Colloidal Quantum Dot Mid-Wave Infrared Photodetectors. *ACS Nano* **2018**, *12* (7), 7264–7271.
- (46) Rastogi, P.; Izquierdo, E.; Gréboval, C.; Cavallo, M.; Chu, A.; Dang, T. H.; Khalili, A.; Abadie, C.; Alchaar, R.; Pierini, S.; Cruguel, H.; Witkowski, N.; Utterback, J. K.; Brule, T.; Xu, X. Z.; Hollander, P.; Ouerghi, A.; Gallas, B.; Silly, M. G.; Lhuillier, E. Extended Short-Wave Photodiode Based on CdSe/HgTe/Ag₂Te Stack with High Internal Efficiency. *J. Phys. Chem. C* **2022**, *126* (32), 13720–13728.
- (47) Qu, J.; Weis, M.; Izquierdo, E.; Mizrahi, S. G.; Chu, A.; Dabard, C.; Gréboval, C.; Bossavit, E.; Prado, Y.; Péronne, E.; Ithurria, S.; Patriarche, G.; Silly, M. G.; Vincent, G.; Boschetto, D.; Lhuillier, E. Electroluminescence from Nanocrystals above 2 μm . *Nat. Photonics* **2022**, *16* (1), 38–44.
- (48) Shen, X.; Peterson, J. C.; Guyot-Sionnest, P. Mid-Infrared HgTe Colloidal Quantum Dot LEDs. *ACS Nano* **2022**, *16* (5), 7301–7308.
- (49) Zhang, Z.; Yates, J. T. Jr. Band Bending in Semiconductors: Chemical and Physical Consequences at Surfaces and Interfaces. *Chem. Rev.* **2012**, *112* (10), 5520–5551.
- (50) Lan, X.; Chen, M.; Hudson, M. H.; Kamysbayev, V.; Wang, Y.; Guyot-Sionnest, P.; Talapin, D. V. Quantum Dot Solids Showing State-Resolved Band-like Transport. *Nat. Mater.* **2020**, *19* (3), 323–329.
- (51) Allan, G.; Delerue, C. Tight-Binding Calculations of the Optical Properties of HgTe Nanocrystals. *Phys. Rev. B* **2012**, *86* (16), 165437.
- (52) Kang, I.; Wise, F. W. Electronic Structure and Optical Properties of PbS and PbSe Quantum Dots. *JOSA B* **1997**, *14* (7), 1632–1646.

- (53) Xing, Y.; Yazdani, N.; Lin, W. M. M.; Yarema, M.; Zahn, R.; Wood, V. Effect of Positional Disorders on Charge Transport in Nanocrystal Quantum Dot Thin Films. *ACS Appl. Electron. Mater.* **2022**, 4 (2), 631–642.
- (54) Rastogi, P.; Chu, A.; Dang, T. H.; Prado, Y.; Gréboval, C.; Qu, J.; Dabard, C.; Khalili, A.; Dandeu, E.; Fix, B.; Xu, X. Z.; Ithurria, S.; Vincent, G.; Gallas, B.; Lhuillier, E. Complex Optical Index of HgTe Nanocrystal Infrared Thin Films and Its Use for Short Wave Infrared Photodiode Design. *Adv. Opt. Mater.* **2021**, 9 (10), 2002066.

TOC graphic

